CrossMark

Observation and Modeling of High-temperature Solar Active Region Emission during the High-resolution Coronal Imager Flight of 2018 May 29

Harry P. Warren[1] , Jeffrey W. Reep[1] , Nicholas A. Crump[1], Ignacio Ugarte-Urra[1] , David H. Brooks[2,3] ,
Amy R. Winebarger[4] , Sabrina Savage[4] , Bart De Pontieu[5,6] , Hardi Peter[7] , Jonathan W. Cirtain[8] , Leon Golub[9] ,
Ken Kobayashi[4], David McKenzie[4], Richard Morton[10] , Laurel Rachmeler[4] , Paola Testa[9] , Sanjiv Tiwari[5,11] , and
Robert Walsh[12]

[1] Space Science Division, Naval Research Laboratory, Washington, DC 20375, USA
[2] College of Science, George Mason University, 4400 University Drive, Fairfax, VA 22030, USA
[3] Hinode Team, ISAS/JAXA, 3-1-1 Yoshinodai, Chuo-ku, Sagamihara, Kanagawa 252-5210, Japan
[4] NASA Marshall Space Flight Center, 320 Sparkman Drive NW, Huntsville, AL 35805, USA
[5] Lockheed Martin Solar and Astrophysics Laboratory, 3251 Hanover Street, Palo Alto, CA 94304, USA
[6] Institute of Theoretical Astrophysics, University of Oslo, P.O. Box 1029 Blindern, NO-0315 Oslo, Norway
[7] Max Planck Institute for Solar System Research, D-37077 Göttingen, Germany
[8] BWX Technologies, Inc., 800 Main Street #400, Lynchburg, VA 24504, USA
[9] Harvard-Smithsonian Center for Astrophysics, 60 Garden Street, Cambridge, MA 02138, USA
[10] Mathematics, Physics and Electrical Engineering, Northumbria University, Newcastle Upon Tyne NE1 8ST, UK
[11] Bay Area Environmental Research Institute, NASA Research Park, Moffett Field, CA 94035, USA
[12] Jeremiah Horrocks Institute, University of Central Lancashire, Preston, PR1 2HE, UK

Abstract

Excellent coordinated observations of NOAA active region 12712 were obtained during the flight of the High-resolution Coronal Imager (Hi-C) sounding rocket on 2018 May 29. This region displayed a typical active region core structure with relatively short, high-temperature loops crossing the polarity inversion line and bright "moss" located at the footpoints of these loops. The differential emission measure (DEM) in the active region core is very sharply peaked at about 4 MK. Further, there is little evidence for impulsive heating events in the moss, even at the high spatial resolution and cadence of Hi-C. This suggests that active region core heating is occurring at a high frequency and keeping the loops close to equilibrium. To create a time-dependent simulation of the active region core, we combine nonlinear force-free extrapolations of the measured magnetic field with a heating rate that is dependent on the field strength and loop length and has a Poisson waiting time distribution. We use the approximate solutions to the hydrodynamic loop equations to simulate the full ensemble of active region core loops for a range of heating parameters. In all cases, we find that high-frequency heating provides the best match to the observed DEM. For selected field lines, we solve the full hydrodynamic loop equations, including radiative transfer in the chromosphere, to simulate transition region and chromospheric emission. We find that for heating scenarios consistent with the DEM, classical signatures of energy release, such as transition region brightenings and chromospheric evaporation, are weak, suggesting that they would be difficult to detect.

Unified Astronomy Thesaurus concepts: Solar corona (1483)

1. Introduction

Understanding how the solar atmosphere is heated to high temperatures is one of the most compelling unsolved problems in astrophysics. This process is undoubtedly driven by the turbulent motions of the photosphere, but the detailed physics of how this energy is carried by the magnetic field and ultimately dissipated is not yet understood. Current theories of coronal heating suggest that this dissipation occurs on spatial and temporal scales far below current observational capabilities (e.g., Klimchuk 2006), and it is a significant challenge to use the observations to constrain theoretical models.

Historically, considerable effort has gone into quantifying the temperature structure of coronal loops (see Reale 2014 for a review). The logic behind this approach is that the distribution of temperatures contains information on the magnitude and frequency of the heating events. If heating events are relatively infrequent relative to a cooling time, then each event will be larger in magnitude, leading to broad temperature distributions as loops are heated and cool through a wide range of temperatures (e.g., Cargill 1994). Smaller, more frequent events, in contrast, would lead to loops that are close to

equilibrium and have relatively narrow temperature distributions. Of course, the superposition of many loops along the line of sight complicates this simple interpretation.

Numerical models of coronal heating based on wave dissipation (e.g., van Ballegooijen et al. 2011; Asgari-Targhi & van Ballegooijen 2012; van Ballegooijen et al. 2017) generally indicate high-frequency heating. Simulations based on magnetic reconnection, in contrast, are driven at comparably lower frequencies (e.g., Gudiksen & Nordlund 2005; Bingert & Peter 2011; Hansteen et al. 2015; Dahlburg et al. 2016). The significant difference between the magnetic Reynolds number of the solar corona and the values achievable in numerical simulations, however, makes these theoretical results difficult to interpret. Further, the distinction between heating by magnetic reconnection and waves is likely to be blurred by the fact that reconnection excites waves (e.g., Kigure et al. 2010).

Observational studies have generally indicated relatively narrow temperature distributions in coronal structures. This is true for both the long, approximately 1 MK loops that are commonly found at the edges of active regions (e.g., Lenz et al. 1999; Aschwanden et al. 2000; Del Zanna & Mason 2003;

Warren et al. 2008) and the short, approximately 4 MK loops that occupy the active region core (e.g., Saba & Strong 1986; Schmelz et al. 1996; Warren et al. 2011, 2012; Del Zanna 2014; Del Zanna et al. 2015).

In this paper, we attempt to form a self-consistent picture of the high-temperature active region core emission by combining observations, magnetic field extrapolations, and hydrodynamic simulations. Our focus is on NOAA active region 12712 observed during the second successful flight of the High-resolution Coronal Imager (Hi-C; Kobayashi et al. 2014; Rachmeler et al. 2019) sounding rocket on 2018 May 29. During the flight, Hi-C took very high spatial ($\approx 0\rlap{.}''3$–$0\rlap{.}''4$ or 220–290 km) and temporal (≈ 4.4 s) resolution observations in a bandpass that features the Fe IX 171 Å line as well as lower-temperature O V and O VI lines. Coordinated observations from the Interface Region Imaging Spectrograph (IRIS; De Pontieu et al. 2014) provide measurements of the chromosphere and lower transition region. In combination, these measurements provide a unique view of the active region "moss" (e.g., Berger et al. 1999), the footpoints of the high-temperature active region core loops. Coordinated observations from the EUV Imaging Spectrometer (EIS; Culhane et al. 2007), the X-ray Telescope (XRT; Golub et al. 2007), and the Atmospheric Imaging Assembly (AIA; Lemen et al. 2012) provide the measurements needed to infer the distribution of temperatures and the temporal variability in the active region core.

We find that the EIS, AIA, and XRT observations of the active region core analyzed here yield a differential emission measure distribution (DEM) that is sharply peaked near 4 MK. Between 4 and 8 MK, the magnitude of the DEM falls by more than a factor of 100, suggesting that the amount of plasma heated to very high temperatures is generally small. Further, the Hi-C measurements for this flight show very little evidence for impulsive heating events in the moss. During the first flight of Hi-C, Testa et al. (2013) reported transient brightenings in the AIA Fe XVIII 94 Å channel that were associated with rapidly evolving moss intensities in the 193 Å Hi-C bandpass, and Testa et al. (2014, 2020) found several similar events in IRIS observations, but such events are not detected here. In the data set analyzed in this paper, some transient events are observed in the IRIS spectroscopic observations, but these events do not appear to be directly linked to coronal activity. Our results suggest that active region core heating can occur at a relatively high frequency, consistent with the analysis of lower-resolution and lower-cadence observations (Berger et al. 1999; Antiochos et al. 2003).

To model the active region core emission, we combine extrapolations of the photospheric vector magnetic field measured by the Helioseismic and Magnetic Imager (HMI; Scherrer et al. 2012) with a volumetric heating rate that is a function of the field strength and loop length and has a Poisson waiting time distribution. We find that simulations with relativity high-frequency heating provide the closest match to the observational constraints. Our prescription for the heating closely follows Cargill (2014) and Cargill et al. (2015), and our results are largely consistent with those earlier studies.

Finally, we investigate the response of the lower atmosphere to the high-frequency heating scenario implied by the full active region modeling using the HYDrodynamics and RADiation code (HYDRAD; e.g., Bradshaw & Mason 2003). This code has recently been updated to include the effects of nonlocal thermodynamic equilibrium on the level populations

(Reep et al. 2019), making it possible to study the hydrodynamic response of the lower transition region and chromosphere in multi-threaded models. These simulations generally indicate that for heating scenarios consistent with the active region core DEM, the classical signatures of the heating, such as strong intensity variations and evaporative upflows, are generally very weak, suggesting that they would be difficult to detect.

2. Observations

NOAA active region 12712, which is shown in Figure 1, had a relatively simple bipolar magnetic structure. As we will see, this gave rise to short, high-temperature loops in the active region core (also see, e.g., Tiwari et al. 2019) and longer, somewhat cooler loops on the periphery of the active region. In this section we give a brief overview of the observations from each instrument and describe the preparation of the data. The general purpose routines mentioned here are available as part of the SolarSoftware distribution (Freeland & Handy 1998).

2.1. AIA

The AIA instrument on the Solar Dynamics Observatory is a set of normal incidence, multilayer telescopes that take full-Sun images in a number of EUV and UV bandpasses at relatively high spatial ($0\rlap{.}''6$ plate scale) and temporal (12 or 24 s) resolutions. The point-spread function for AIA is approximately 1000 km FWHM, and depends on the wavelength (Brooks et al. 2012; Grigis et al. 2012). Cutouts of the full-disk images can be obtained from the Stanford Joint Science Operations Center (JSOC) Science Data Processing (SDP) center.[13] We centered the cutouts on the Hi-C field of view and requested data for an hour around the time of the Hi-C launch. We used aia_prep to process the data to a common plate scale and custom routines to organize the images into co-aligned data cubes. An example set of AIA EUV cutout images is shown in Figure 2.

We use the AIA images as an absolute pointing reference. The cross correlation of the AIA EUV images suggests that the internal co-alignment is good to less than a single spatial pixel for the 94, 131, 171, and 193 channels. Somewhat larger offsets of 1–2 pixels are evident in the 211 and 335 channels. This level of consistency is sufficient for working with lower-resolution data from EIS and XRT.

The AIA 94 channel contains the Fe XVIII 93.96 Å emission line, which has a peak temperature of formation at about 8 MK, and is particularly important for studying heating in active regions (e.g., Testa & Reale 2012; Ugarte-Urra & Warren 2014). As we will see, most of the emission in this line comes from plasma at a much lower temperature. Unfortunately, this line is blended with lower-temperature emission (e.g., Fe XIV, Del Zanna 2013a; Fe IX, Testa et al. 2012b) for which there is often limited atomic data. For this reason empirical approaches have been developed that use other channels to infer the contribution of the lower-temperature emission and subtract it off (Teriaca et al. 2012; Warren et al. 2012; Del Zanna 2013a). This is illustrated in the lower rightmost two panels of Figure 2.

Since the empirical corrections to the 94 channel were derived using data from early in the mission, we use the routine

---

[13] http://jsoc.stanford.edu/ajax/lookdata.html
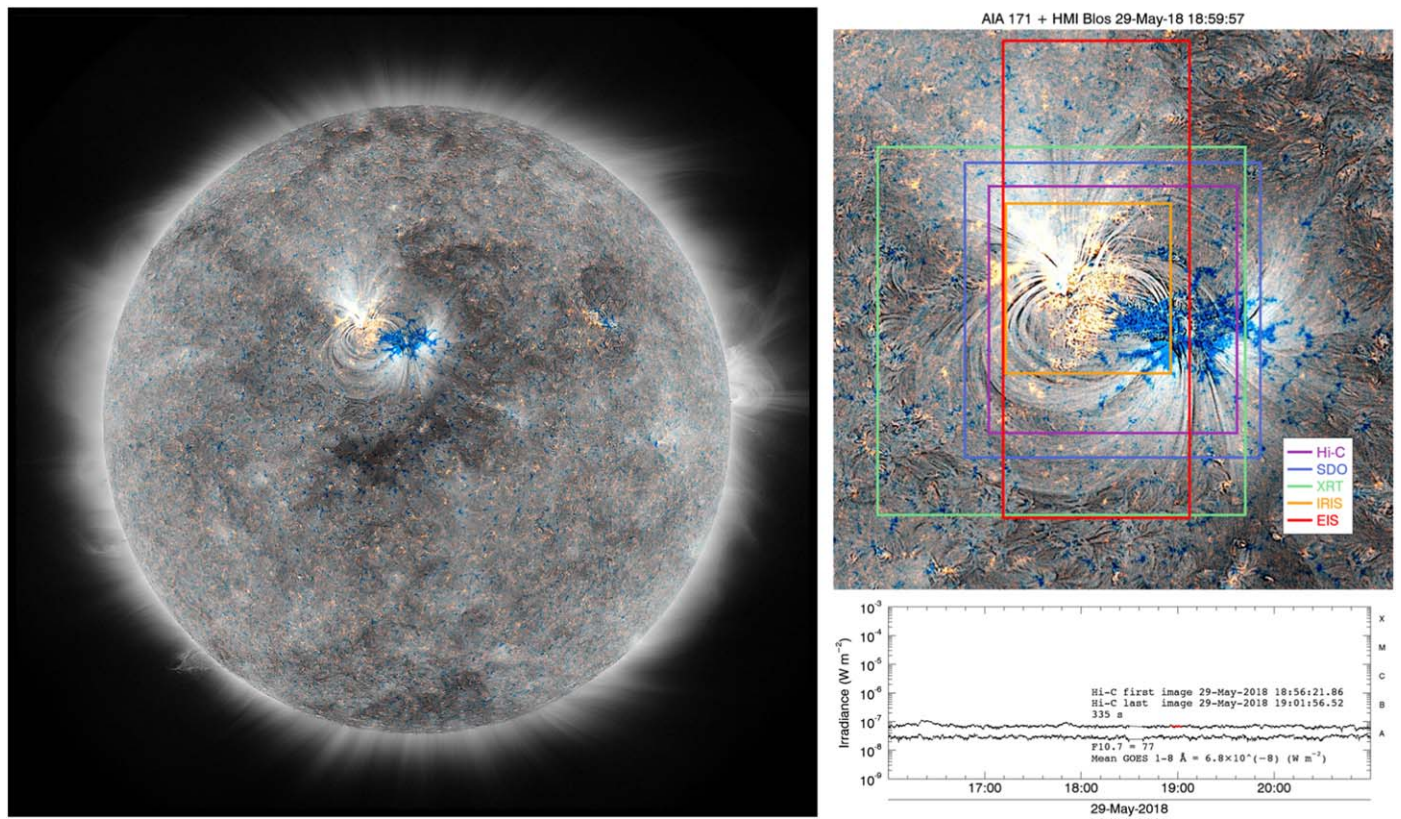
Figure 1. A summary of observations taken during the Hi-C flight of 2018 May 29. (Left panel) A composite image that combines an HMI line-of-sight magnetogram and a sharpened AIA 171 Å image, both taken near 18:59:57 UT. (Top right panel) The approximate fields of view for Hi-C, EIS, XRT, IRIS, the AIA cutout, and the HMI cutout are shown on the composite image. (Bottom right panel) GOES 1–8 and 0.5–4 Å light curves. The times of the Hi-C flight are indicated in the plot.
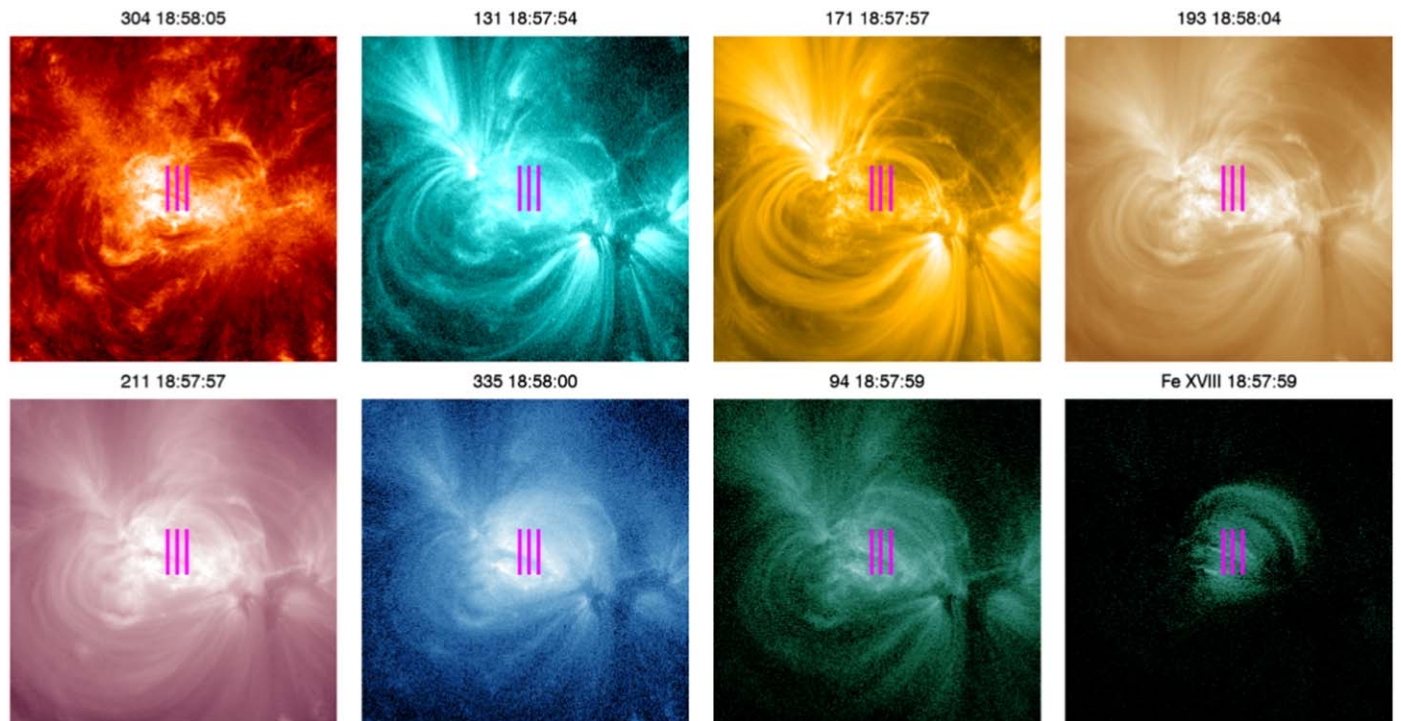
Figure 2. Representative AIA EUV images taken during the Hi-C flight. The vertical lines indicate the EIS slit positions used to compute the active region core intensities. The 94 channel has been processed to remove the warm emission and isolate the contribution of Fe XVIII (see the final two panels).
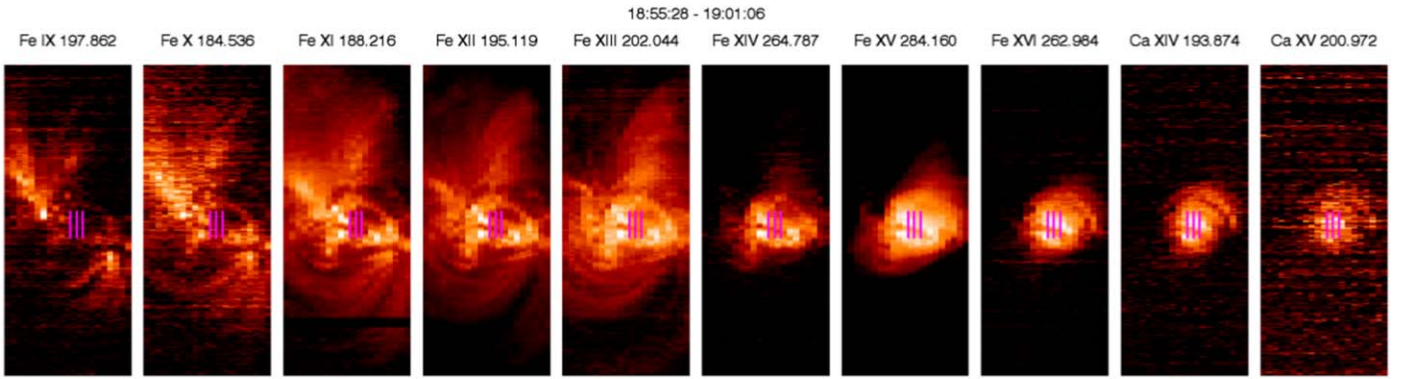
Figure 3. Examples of coarse EIS rasters taken during the Hi-C flight. These rasters covered an area of 200″ × 512″ using 10″ steps in 360 s. To compute the active region core intensities, the spectra at three slit positions, which are indicated by the vertical lines, were averaged together.

aia_bp_get_corrections to correct the observed intensities for sensitivity loss. We use CHIANTI v9.0.1 (Dere et al. 2019) and the routine ch_aia_resp to compute updated temperature responses for all of the AIA EUV channels. Since we have corrected the observed intensities, we turn off the time-dependent correction to the effective areas. We also use the evenorm correction to bring the AIA observations into agreement with irradiance observations from the Extreme Ultraviolet Variability Experiment (EVE; Woods et al. 2012; also see Boerner et al. 2014). Further, we modified the routine to compute the response for the 94 channel including only the contributions of Fe XVIII and the continuum. The AIA responses have been computed assuming the "coronal" abundances of Feldman (1992), consistent with previous emission measure analysis of these high-temperature active region core loops (e.g., Del Zanna 2013a).

2.2. EIS

The EIS instrument on Hinode provides spectroscopic observations in two spectral ranges, 171–212 Å and 245–291 Å, with a spectral resolution of about 22 mÅ and a spatial pixel size of about 1″. The point-spread function for EIS is approximately 1800 km FWHM (Brooks et al. 2012). Solar images can be made by stepping the slit over a region of the Sun and taking an exposure at each position. Relatively strong emission lines from Fe VIII–Fe XVI and Ca XIV–Ca XVII allow for excellent temperature resolution below temperatures of about 5 MK.

During the Hi-C launch window, EIS took "fast scan" rasters with relatively short exposures (15 s) and very large (10″) steps between positions. Each of these coarse rasters covered an area of 200″ × 512″ and took about 360 s to complete. An example set of rasters is shown in Figure 3. Additional rasters with deeper exposures and smaller steps were taken outside of the launch window. These rasters are useful for probing some of the moss properties at higher spatial resolutions. To determine the line intensities in all of these rasters, the profile at each spatial position was fit with a Gaussian. The absolute intensities were corrected for changes from the pre-flight calibration using the results from Warren et al. (2014). For these averaged spectra, the uncertainty in the absolute calibration dominates the counting statistics. Unfortunately, the uncertainty in the calibration is difficult to represent with a single number. The relative uncertainty for two lines close in wavelength, for example, is likely to be much less than two lines separated widely in wavelength. Del Zanna (2013b) also examined the

changes in the EIS calibration over time. Applying these corrections yields intensities that differ by about 25% from what we have used and provide a measure of the relative uncertainties in the absolute calibration. These uncertainties are small relative to the large variations in emission measure that we are interested in.

Our primary interest for this study is in the properties of the hot active region core loops and the corresponding moss. To improve the signal-to-noise ratio, we have averaged the EIS spectra where the Ca XIV 193.874 Å emission is brightest and determined the intensities from fits to these averaged profiles. The EIS slit positions used for the averaging are indicated by the vertical magenta lines in Figures 2–6.

Since the spacing between the exposures in the EIS rasters is large, we need to extract the intensities from the image data from the same vertical slices, rather than simply averaging over a box. To co-align EIS and AIA, we considered the 195 Å intensities along the slit in each EIS exposure and cross correlated them with a range of spatial positions in the corresponding AIA 193 Å image to find the best match. To improve the co-alignment, we convolved the EIS spectra with the AIA 193 Å effective area and smoothed and downsampled the AIA images to the lower spatial resolution of EIS. See Warren et al. (2016) for additional details and examples. The result of this calculation is a mapping from EIS pixel coordinates to absolute coordinates as measured by AIA. Finally, all of the atomic data used for interpreting the EIS intensities comes from CHIANTI version 9.0.1 (Dere et al. 2019). To enable rapid DEM calculations, we have pre-computed the emissivities for many of the EIS lines over a grid of temperatures and densities. We can then interpolate to determine the emissivity for specific input parameters. As discussed previously, we assume the "coronal" abundances of Feldman (1992) for these calculations.

2.3. XRT

The XRT instrument on Hinode is a grazing incidence telescope that takes broadband, soft X-ray images of the Sun with a spatial resolution of about 1″. End-to-end tests on the ground and subsequent on-orbit PSF evaluations indicate that the angular resolution is 2″ for a diameter of 50% enclosed energy (Golub et al. 2007). Temperature discrimination is achieved through the use of focal plane filters. XRT complements EIS by providing coverage at temperatures above 5 MK.
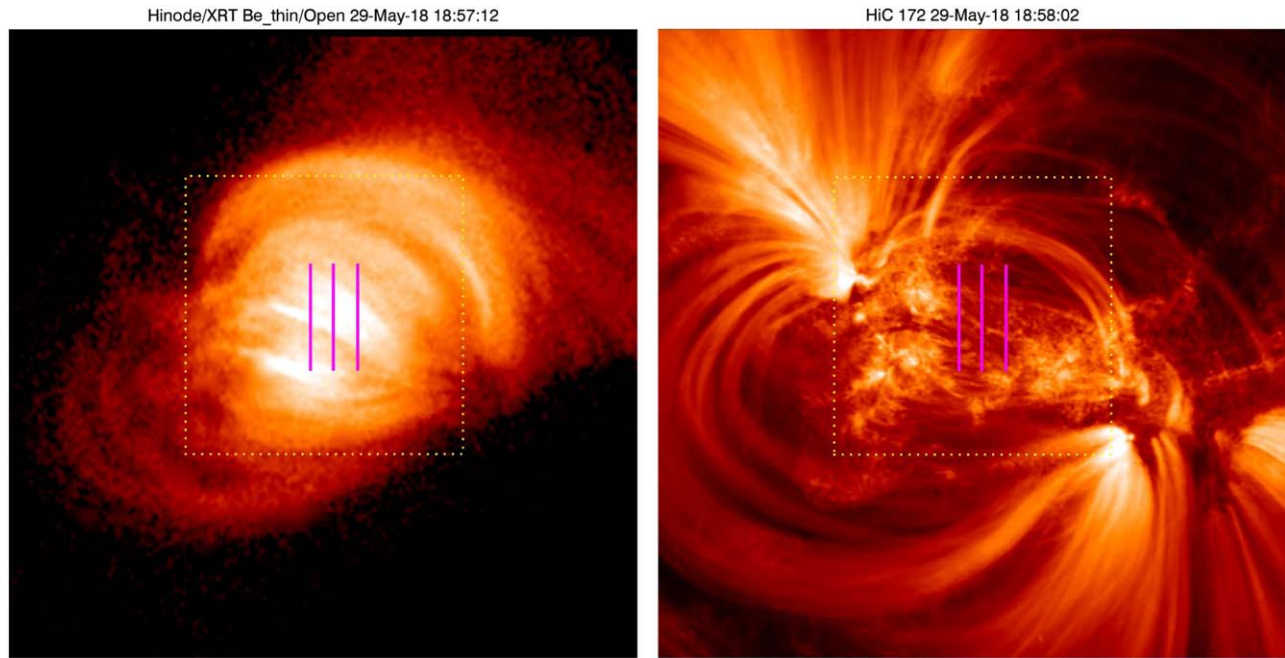
Figure 4. Representative XRT and Hi-C images taken during the flight. The field of view is $250'' \times 250''$. The dotted line indicates the field of view shown in Figure 5. The vertical lines indicate the positions of the EIS slits used for the active region core intensities.
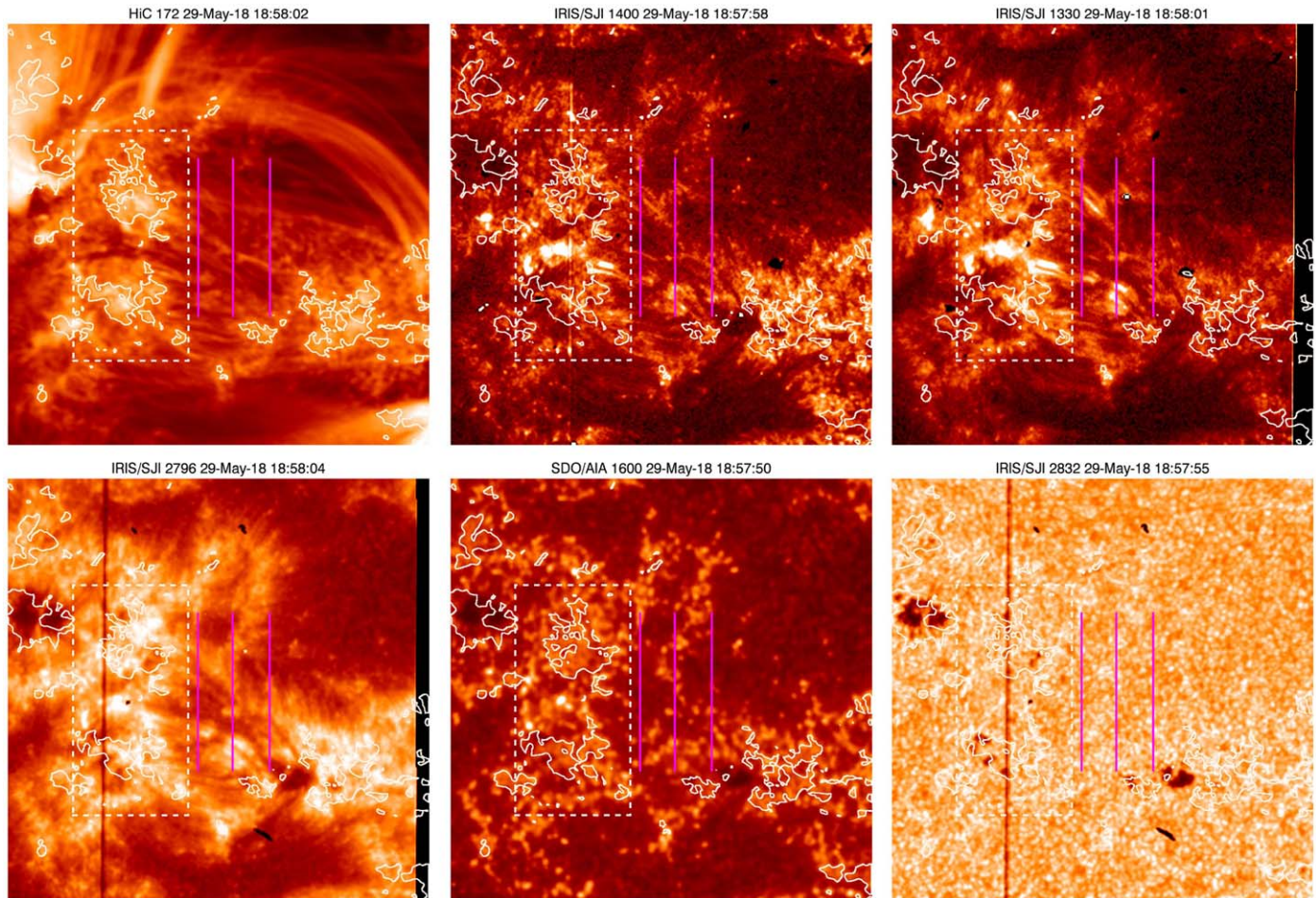
Figure 5. Example Hi-C, IRIS, and AIA 1600 Å images of the active region core taken during the flight. The field of view for each image is $110'' \times 110''$. The vertical feature in the IRIS slit-jaw images indicates the position of the IRIS slit at the time of the exposure. The vertical magenta lines indicate the EIS slit positions used to compute the active region core intensities. The box and contours highlight the moss areas that will be discussed in detail in Section 3.
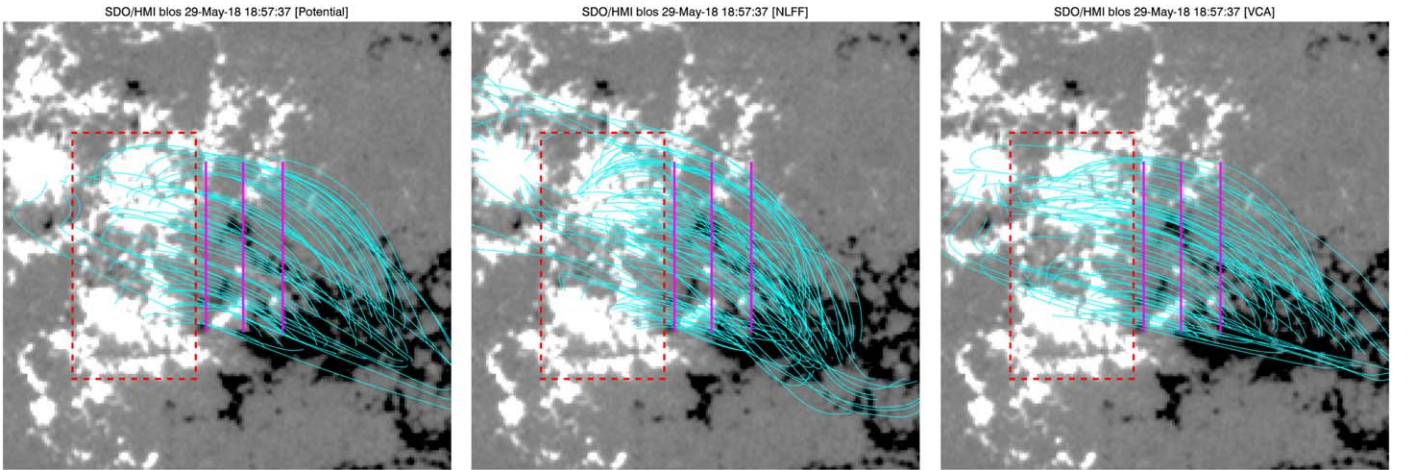
Figure 6. Randomly selected field lines that pass through the EIS slit in the active region core. The position of the EIS slit is indicated by vertical lines. The red box highlights the region of moss that is examined in detail in Figures 8 and 9. The field lines are computed from three different magnetic field extrapolation methods, a potential model (left panel), a nonlinear force-free model driven by measurements of the photospheric magnetic field (center panel), and a model of the topology of loops in the corona (right panel). See Warren et al. (2018) for additional details.

During the Hi-C launch window, XRT cycled over the Al-Poly/Open, Be-Thin/Open, and Be-Med/Open filters with a cadence of about 60 s and a field of view of $384'' \times 384''$. An example image is shown in Figure 4. XRT images were co-aligned to AIA using cross correlation with the processed AIA Fe XVIII images.

The time-dependent XRT temperature response was computed using the standard routines make_xrt_wave_resp and make_xrt_temp_resp and the APEC_DEFAULT atomic data. We note that it is necessary to scale the computed XRT responses by a factor of two to bring them into agreement with the AIA 94 Å channel (see Section 4 of Mitra-Kraev & Del Zanna 2019 for an extensive discussion of this issue.)

2.4. Hi-C

Hi-C is a normal incidence imager similar to AIA in design, but with higher spatial resolution ($0''.129$ plate scale) and higher throughput (≈ 4.4 s cadence). For this flight, the optics were coated with a multilayer that isolated the Fe IX 171 Å line.

We use the Level1.5 Hi-C data that has been co-registered to the AIA 171 Å channel. To simplify the analysis, we rotate the Hi-C images to account for the roll relative to AIA ($\sim 0°.985$). To further refine the absolute pointing, we have cross correlated each rotated Hi-C image with the closest AIA cutout image in time. Since AIA and Hi-C images have different plate scales, they must be resampled to a common resolution before the cross correlation can be calculated. We have chosen to interpolate the AIA images to match Hi-C, which simplifies the comparison of light curves from the different instruments.

An example Hi-C image is shown in Figure 4. As noted in the instrument paper, these Hi-C images show evidence for a quasiperiodic motion blur (see Section 3.2 of Rachmeler et al. 2019). For this study, our primary interest is in the dynamics of the active region footpoints at high spatial resolution and cadence. As we will see, the motion blur does appear to impact the light curves derived from the moss emission. For the images not affected by motion blur, the spatial resolution is between $0''.3$ and $0''.47$ (Rachmeler et al. 2019).

2.5. IRIS

IRIS is a compact spectrograph based on a Cassegrain design. Special coatings allow for simultaneous imaging of the 1332–1407 and 2783–2835 Å wavelength ranges. The far-UV (FUV) wavelength range includes strong emission lines from O I 1355.598, C II 1334.535 and 1335.708, Si IV 1393.755 and 1402.770, O IV 1399.775 and 1401.163, Fe XII 1349.382, and Fe XXI 1354.080 Å. The near-UV (NUV) wavelength range includes the Mg II k 2796 and Mg II 2803 Å lines. Spectrally resolved observations are provided by passing solar radiation through a $0''.33 \times 175''$ slit and reflecting it off of a grating. The resulting spectral resolution is about 26 mÅ in the FUV and 53 mÅ in the NUV. Light reflected off of the slit assembly is passed through one of four science filters to allow for context imaging of an area $175'' \times 175''$ around the slit. The nearly 7 m effective focal length provides a plate scale of $0''.33$ or about 230 km. An on-orbit analysis indicates that the FUV spectrograph and slit-jaw imager spatial resolution is pixel limited ($0''.33$) and the NUV spectrograph and slit-jaw imager have a spatial resolution of about $0''.4$ (De Pontieu et al. 2014; Courrier et al. 2018).

During the Hi-C launch window, IRIS executed a series of eight position rasters over an $8'' \times 175''$ field of view in the moss. The time between exposures was about 3 s, and the time between successive rasters scans was about 25 s. Seven spectral windows were selected for telemetry. Slit-jaw images were taken in 1330, 1400, 2796, and 2832 Å with about 13 s between the images in a given wavelength. An example set of IRIS slit-jaw images is shown in Figure 5.

2.6. HMI

HMI provides both vector and line-of-sight measurements of the photospheric magnetic field over the full solar disk with a plate scale of about $0''.5$ and a cadence ranging between 45 s and 720 s, depending on the type of measurement.

Cutouts of the HMI line-of-sight, continuum, and vector field data were downloaded from the JSOC and organized into co-aligned data cubes. The parameters for the cutouts were matched to those used for the AIA images. aia_prep was used to interpolate the HMI data onto the same scale as the AIA

images. An example HMI line-of-sight field measurement in the active region core is shown Figure 6.

3. Properties of the Active Region Core

In this section we will discuss the hot, active region core loops using the EIS, AIA, and XRT observations to determine the temperature structure near the loop apex and Hi-C and IRIS to determine the temporal variability near the loop footpoints. As we will see, there are many ambiguities in interpreting the various observations and models. It is not clear, for example, exactly which regions in the Hi-C or IRIS images correspond to the footpoints of the high-temperature, active region core loops. It is not clear how we should measure the variability in the footpoints or what level of variability a given model predicts. How to compute the temperature distribution for the active region core and account for all of the uncertainties is also difficult. In this section we address all of these issues. In the next section we will compute hydrodynamic simulations for the high-temperature loops and compare the simulation results with the observations. As we will see, despite the many ambiguities, the observations and the simulations, taken together, paint a self-consistent picture of high-frequency heating in the active region core loops.

3.1. Magnetic Field Extrapolations

To understand the general topology of the active region core loops that pass through the EIS slit (as indicated by the vertical lines in Figures 2–6), we trace magnetic field lines and select those whose projection on the solar disk intersects at least one point on the EIS slit. To compute the field lines, we use three different models, a simple potential model that uses the HMI line-of-sight field as a boundary condition, a nonlinear force-free (NLFF) model that uses HMI vector magnetic field measurements (Wiegelmann 2004), and a nonlinear model that uses the HMI line-of-sight field and introduces Vertical Current Approximation to better match the topology of the observed coronal loops (Aschwanden 2016). Additional details on these extrapolation techniques are discussed in Warren et al. (2018).

Selected active region core field lines are displayed in Figure 6. Here we show a randomly selected subset of field lines with a footpoint field strength above 20 G and a total length below 250 Mm. The constraint on the length removes the larger overlying loops that are unlikely to be at high temperature. As expected (e.g., Tiwari et al. 2017), these field lines are generally rooted in the strong plage field just across from the polarity inversion line. Further, for this case, the different extrapolation methods produce generally similar footpoint locations for the traced field lines.

3.2. Intensity Variability in the Moss

The properties of the heating implied by the high-temperature emission in the active region core should be reflected in the behavior of the footpoints. If these loops really are heated at a high frequency, then we should observe relatively steady emission in the moss, the footpoints of these loops. Such a result was presented by Antiochos et al. (2003), using observations from the Transition Region and Coronal Explorer (TRACE; Handy et al. 1999). Antiochos et al. (2003) concluded that "the heating in the hot moss loops cannot be truly flare-like with a sharp cutoff, but instead must be quasi-steady to an excellent approximation." Similarly, Berger et al. (1999)

concluded that "The intrinsic brightness of individual moss elements varies gradually with some elements appearing to fade in or out of existence on timescales of about 1 minute, with no evidence of impulsive "nano-" or "micro-flaring" as a major energy source for the moss." TRACE, however, had lower spatial resolution ($0\farcs5$ pixels) and much lower cadence (30 s) than Hi-C. Further, Antiochos et al. (2003) saw low variability in the moss when the intensity time series were averaged over $10'' \times 10''$ regions. The higher spatial resolution and higher cadence data from Hi-C should allow us to revisit this question with greatly improved observations.

However, to fully investigate the variability in the moss, we need to confront two questions: (1) which spatial locations belong to the moss? and (2) how do we quantify the variability there?

Historically, moss has been defined by its "spongy, low-lying, appearance" (Berger et al. 1999). Here we would like to explore the properties of individual pixels and need a more precise definition that allows us to segregate and compare moss and non-moss pixels. Since we expect the moss to lie over a strong magnetic field and to be relatively bright, we define an image mask that consists of all points in the active region core with an absolute magnetic field strength above 200 G and an Hi-C intensity above 8000 DN. Contours of this mask are shown in Figures 7–9 and, while they do identify some regions outside of the active region core, they are generally consistent with footpoints of the field lines traced in Figure 6.

To quantify the variability in each spatial pixel, we simply compute the standard deviation in the time history for each point in the Hi-C data cube and normalize it by the median intensity observed over the flight. That is, we compute $\sigma_I(x, y)/\bar{I}(x, y)$. In Figures 7–9, we show a plot of this "variance map" derived from the Hi-C observations. Maps computed from AIA 171 Å produce very similar results. As we will see, this metric is imperfect, but it does serve as a useful guide to the level of activity as a function of position in the active region. An alternative approach would be to identify individual events in the time history of each pixel (e.g., Ugarte-Urra & Warren 2014), but since the flight was short, it would be difficult to train and validate such a model with the limited amount of available data.

Comparing the variance map with the maximum Hi-C intensity along each line of sight, we see that it easily identifies many transient, loop-like structures (Figure 7). These loop-like structures, however, are generally found spanning the polarity inversion line. Focusing on the moss areas identified by the combination of a strong magnetic field and large Hi-C intensity, we generally see very little variability. To further highlight the variability in the moss, in Figures 8 and 9, we show an expanded view of the eastern side of the active region. These figures also show Hi-C and AIA 171 Å light curves for selected pixels.

Many of the pixels in the moss show essentially no variation, as exemplified by light curves 1, 2, and 3. Other pixels (4 and 5) show variability that appears to be caused by the Hi-C jitter. The variability in these pixels is in phase with the jitter (note the different colors for the low- and high-jitter Hi-C images in the light curves) and is also not well correlated with the corresponding AIA signal. The impact of the jitter on a light curve is likely to be related to the structure being measured. For example, a measurement from the middle of a feature that is several pixels in size would show little variation, while a
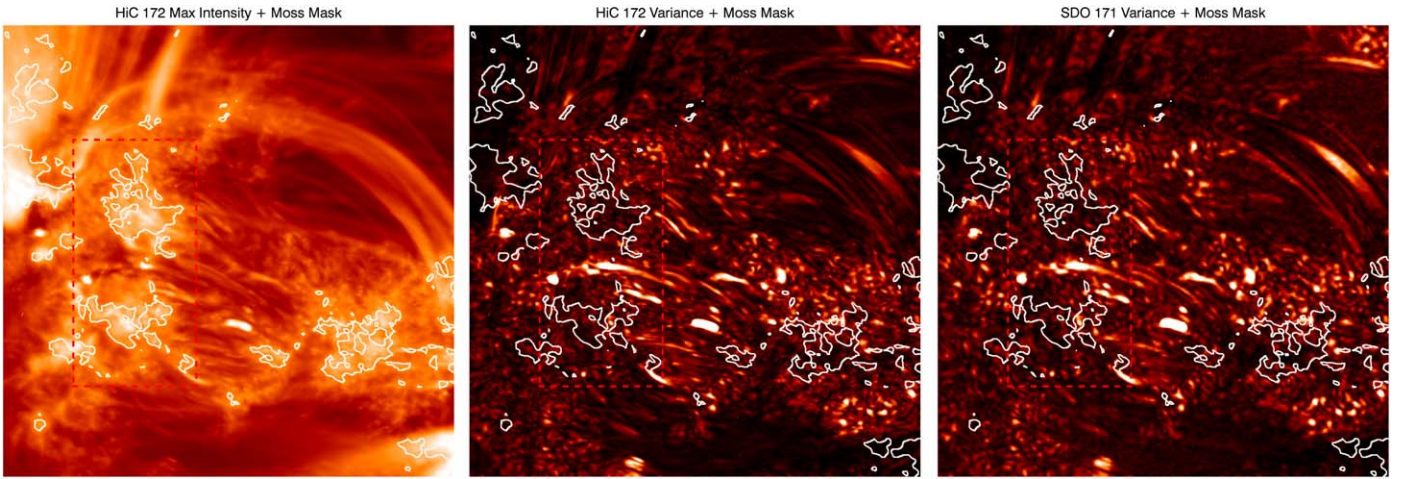
Figure 7. The intensity and variability in the active region core measured with Hi-C. The left panel shows the maximum Hi-C intensity along each line of sight. The center and right panels show the variability in the intensity along each line of sight for Hi-C and AIA 171 Å, respectively. The variability is measured using the standard deviation divided by the median at each position. Also shown are approximate contours of the moss computed from regions where the magnetic field strength is high and the Hi-C intensity is high. The region indicated by the red dotted lines is expanded in Figures 8 and 9.

measurement near the edge of a feature would show significant variation due to the jitter. Some of the observed variability results from secular trends over the 300 s duration of the flight. This behavior is illustrated in light curves 6 and 7. This type of evolution is unlikely to be associated with impulsive heating events. In our survey of the moss pixels, only a few of them, illustrated by light curves 8, 9, and 10, seem to be candidates for impulsive heating events. Pixels such as these exhibit short-lived increases in intensity similar to those discussed by Testa et al. (2013, 2014, 2020).

In total, about 56% of the Hi-C moss pixels in Figures 8 and 9 have a normalized variability of 5% or less (similar to pixels 1–3), and 97% have a variability of 10% or less.

IRIS provides another view into the temporal variability in the moss. Unfortunately, the IRIS observing program for this period is not well suited for the analysis that we performed on the Hi-C data. The IRIS slit-jaw images are at a lower cadence and have somewhat lower signal-to-noise than the Hi-C images. The light curves generally follow the same patterns as are shown in Figures 8 and 9, but with more statistical variation. As mentioned in Section 2.5, IRIS took spectra at eight different positions to form a narrow raster. Even with short (2 s) exposure times, the cadence at each position is about 25 s, much longer than the 4.4 s cadence of Hi-C. Furthermore, since this region is not particularly bright, the short exposures lead to very noisy profiles in almost all of the lines, and only Mg II 2796.354 Å is strong enough to be analyzed in detail. While this line is formed at a much lower temperature than the Fe IX imaged by Hi-C, it does provide an interesting point of comparison for the hydrodynamic models that will be discussed in the next section.

In Figure 10, we show plots of the first three moments of the IRIS Mg II 2796.354 Å profile along with the same field of view in the HMI line-of-sight field and the AIA 1700, 1600, 171, and 304 Å bandpasses. The line intensity is computed by subtracting the continuum at 2795 Å and summing over the profile. The spatial coordinates for the spectra have been adjusted using the mean offsets computed for the slit-jaw images taken during the raster. The panel on the right shows the mean position across the raster as a function of position along the slit. The generally good agreement in these intensities

indicates that the data are well aligned. Finally, to simplify the interpretation of the spectra, we have identified the approximate positions of the moss along the slit. Note that moss contours here are the same as those shown in Figures 5, 7–9.

The time history of each IRIS Mg II 2796.354 Å intensity measured during the Hi-C flight is illustrated in Figure 11. Since variability can be difficult to detect by eye in the absolute intensity, we have also normalized each row (or time series) in these plots by its mean. In contrast to the variability maps for Hi-C, which indicate that a majority of pixels have a variability of 5% or less, these plots suggest pervasive activity. Almost every pixel in the moss shows large ($\pm 30\%$) excursions from the mean intensity over the duration of the Hi-C rocket flight. These events do not appear to be specific to the moss, however; similar events are observed both inside and outside the regions identified as having high-temperature loops. As we will see, numerical simulations of plausible heating scenarios are not consistent with these pervasive, high levels of activity, suggesting that this variability is related to activity originating in the chromosphere, such as spicules.

### 3.3. Active Region Core Temperature Structure

As mentioned in the discussion of the EIS observations, we have computed intensities for the active region core loops using spectra averaged over regions that are bright in Ca XIV 193.874 Å, but generally do not include the moss emission evident in emission formed at 1 MK and below. We also extracted the intensities for these slit positions from the co-aligned AIA and XRT images. The slit positions used for this averaging are indicated in Figures 2–5. For the spectral lines, the uncertainties are computed from the statistical errors on the Gaussian fit parameters. For the image data, we compute the mean and standard deviation of the intensities in the positions along the EIS slit. We estimate the uncertainty in the image intensity as the standard deviation divided by the square root of the number of samples. The complete line list is given in Table 1.

To infer the temperature structure of the observed plasma, we compute the emission measure distribution by inverting the
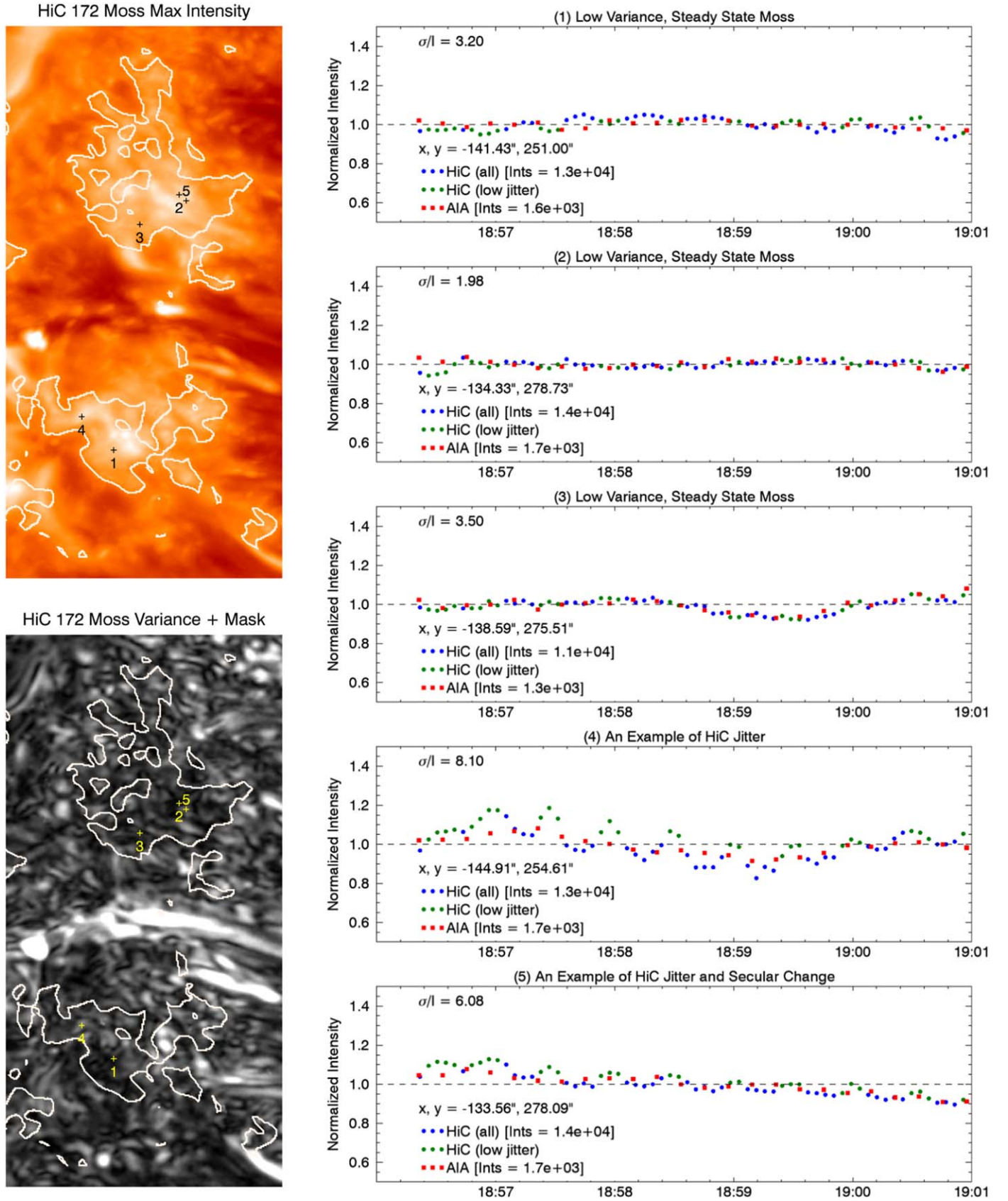
Figure 8. Examples of temporal evolution in the moss observed by Hi-C. The left panels show an expanded view of the maximum intensity and the variability (see Figure 7). The contours show where both the magnetic field and Hi-C intensity are high and give an approximate location of the moss. The right panels show the evolution for selected points. In general, the variability in the moss is low, as is illustrated in pixels 1–3. Some of the observed variance is driven by the quasiperiodic jitter (see pixel 4) or by secular changes in the moss intensity (see pixels 4 and 5).
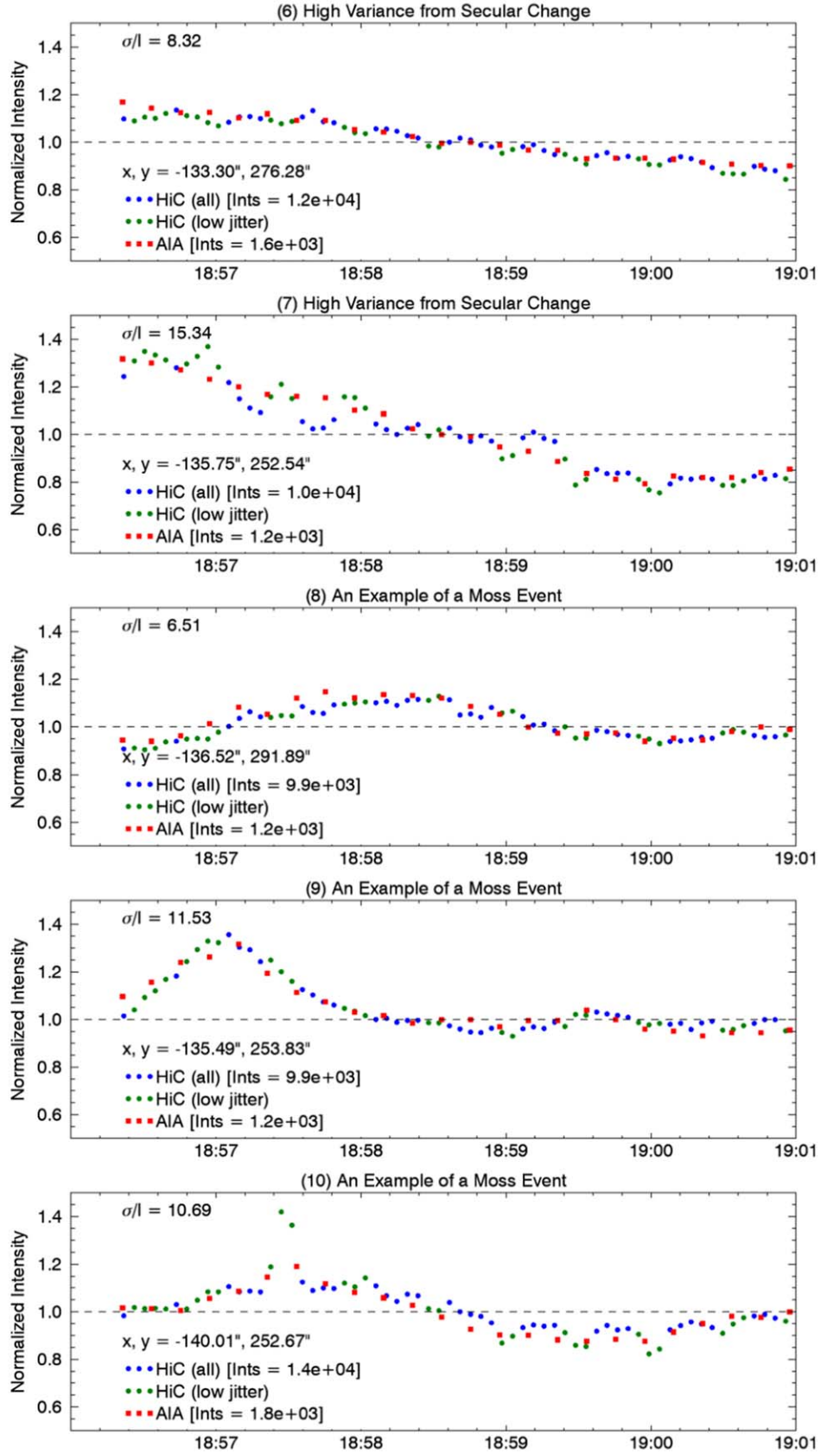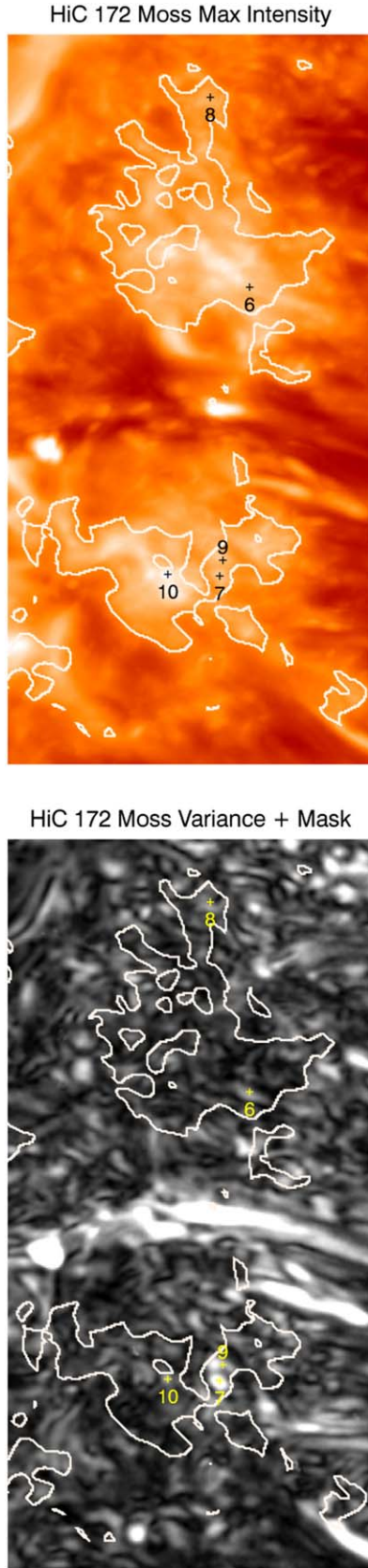
Figure 9. Additional examples of temporal evolution in the moss observed by Hi-C. The format is the same as in Figure 8. Pixels 6 and 7 illustrate variance driven by secular changes in the moss intensity. Pixels 8, 9, and 10 illustrate variability that may be linked to impulsive heating, but such behavior is rare in these observations of the moss.
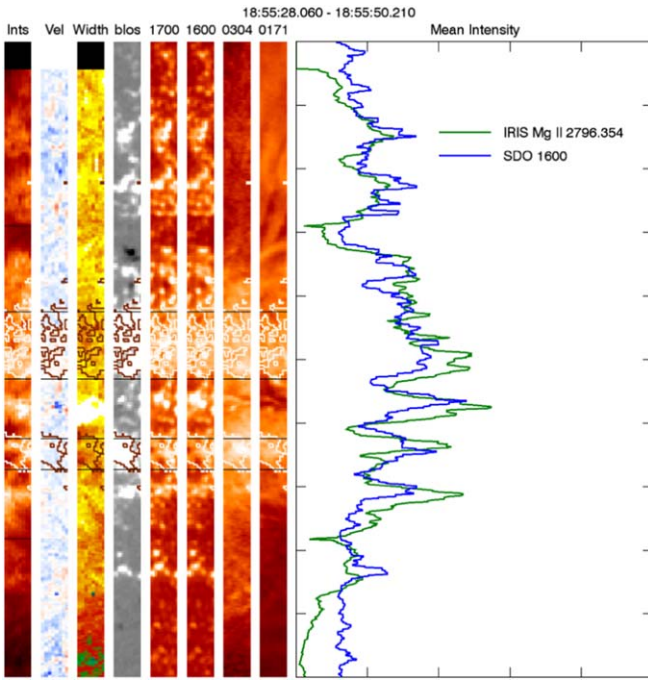
Figure 10. An example IRIS spectral scan taken during the Hi-C flight. The left three panels show the intensity, velocity, and width of Mg II 2796.354. The remaining images show the HMI line-of-sight field, AIA 1700, 1600, 304, and 171. The line plot shows the mean intensity across the raster as a function of position along the slit for both Mg II and 1600. The generally good agreement in these intensities indicates that the spectra and image data are well aligned. The moss mask from the previous images is shown. To simplify the analysis of the spectra, we approximate the moss mask with two horizontal bands, as shown in the image. These bands are also highlighted in Figure 11.

equation

$$I_n = \int \epsilon_n(n_e, T)\xi(T)dT. \qquad (1)$$

Here I_n is the observed intensity in an emission line or imaging bandpass, $\epsilon_n(n_e, T)$ is the corresponding plasma emissivity or temperature response, which is assumed to be known, and $\xi(T) = n_e^2 \, ds/dT$ is the differential emission measure distribution (DEM). Note that, in the figures, we show the emission measure, which is the DEM multiplied by the temperature bin ($dT = 0.02$ dex for these calculations). To solve this equation, we use a modified version of the Bayesian method described in Warren et al. (2017). In this method we represent the DEM as a sum of Gaussian basis functions and assume a Cauchy prior on the weights. This choice of prior biases the solution to be sparse, with only a few nonzero weights. In Warren et al. (2017), we assumed that the weights were of the form 10^w to ensure positivity and performed a full sampling of the posterior, which was very time consuming. Here we assume that the DEM is a simple linear combination of the basis functions and use the BFGS algorithm (Byrd et al. 1995; Zhu et al. 1997) implemented in scipy.optimize to perform a bounded optimization that excludes negative weights. These changes accelerate the calculation by several orders of magnitude. This, and other optimizations under development, will be presented in a future publication.

The resulting DEM is shown in Figure 12 and shows a sharp peak around 3–4 MK. This behavior is very similar to previous

Table 1
Intensities in the Active Region Core

| Instrument	Line/Channel	I_{obs}	I_{err}
EIS	Si VII 275.368	40.02	5.99
EIS	Fe IX 188.497	40.76	2.65
EIS	Fe IX 197.862	27.16	1.37
EIS	Fe X 184.536	271.07	8.65
EIS	Fe XI 188.216	456.01	4.54
EIS	Fe XII 195.119	993.64	4.86
EIS	Fe XIII 202.044	721.94	6.07
EIS	Fe XIII 203.826	918.21	9.33
EIS	Fe XIV 270.519	866.55	11.46
EIS	Fe XIV 264.787	1566.44	14.84
EIS	Fe XV 284.160	11018.92	57.75
EIS	Fe XVI 262.984	1321.13	13.52
EIS	Ca XIV 193.874	138.04	1.75
EIS	Ca XV 200.972	71.48	2.84
AIA	94	10.19	0.17
AIA	131	37.70	0.56
AIA	171	482.25	6.96
AIA	193	933.53	14.17
AIA	211	623.74	8.34
AIA	304	695.83	15.07
AIA	335	85.95	1.06
AIA	Fe XVIII	6.16	0.14
XRT	Al-poly/Open	2274.13	34.90
XRT	Be-med/Open	67.44	1.04
XRT	Be-thin/Open	370.78	5.63

Note. The units for the EIS intensities are erg cm^{-2} s^{-1} sr^{-1}. The units for AIA and XRT are DN s^{-1}. The EIS and AIA intensities have been corrected for sensitivity loss. The XRT responses are adjusted for sensitivity loss, so the intensities have not been corrected. These uncertainties reflect only the counting statistics and do not reflect the uncertainties in the absolute calibration. See Section 2.2 for a discussion of the relative uncertainties in the absolute EIS intensities.

results from active region core measurements (e.g., Warren et al. 2011, 2012; Del Zanna 2013a, 2014; Ishikawa & Krucker 2019), with steep declines in emission measure away from the peak.

The emission measure offers a potentially important constraint on the timescale between heating events. If the heating in these high-temperature, active region core loops occurred at a low frequency, with events spaced at intervals much longer than a cooling time, we should observe a broad distribution of temperatures as individual loops evolve over a broad range of temperatures. Temperature distributions such as this one, however, suggest that the heating must be at a relatively high frequency so that the loops are close to equilibrium and the distribution of temperatures is narrow. We will explore this in more detail in the modeling section, where we perform hydrodynamic simulations using various forms for the heating rate.

4. Hydrodynamic Modeling

In this section we describe the hydrodynamic modeling of an ensemble of loops that represent the active region core. As has been done in many previous studies, the loop properties will be used to inform the magnitude of the heating. Further, motivated by Cargill (2014), who showed that the temperature distribution is sensitive to the time between heating events, we consider time-dependent heating scenarios. The goal here is to
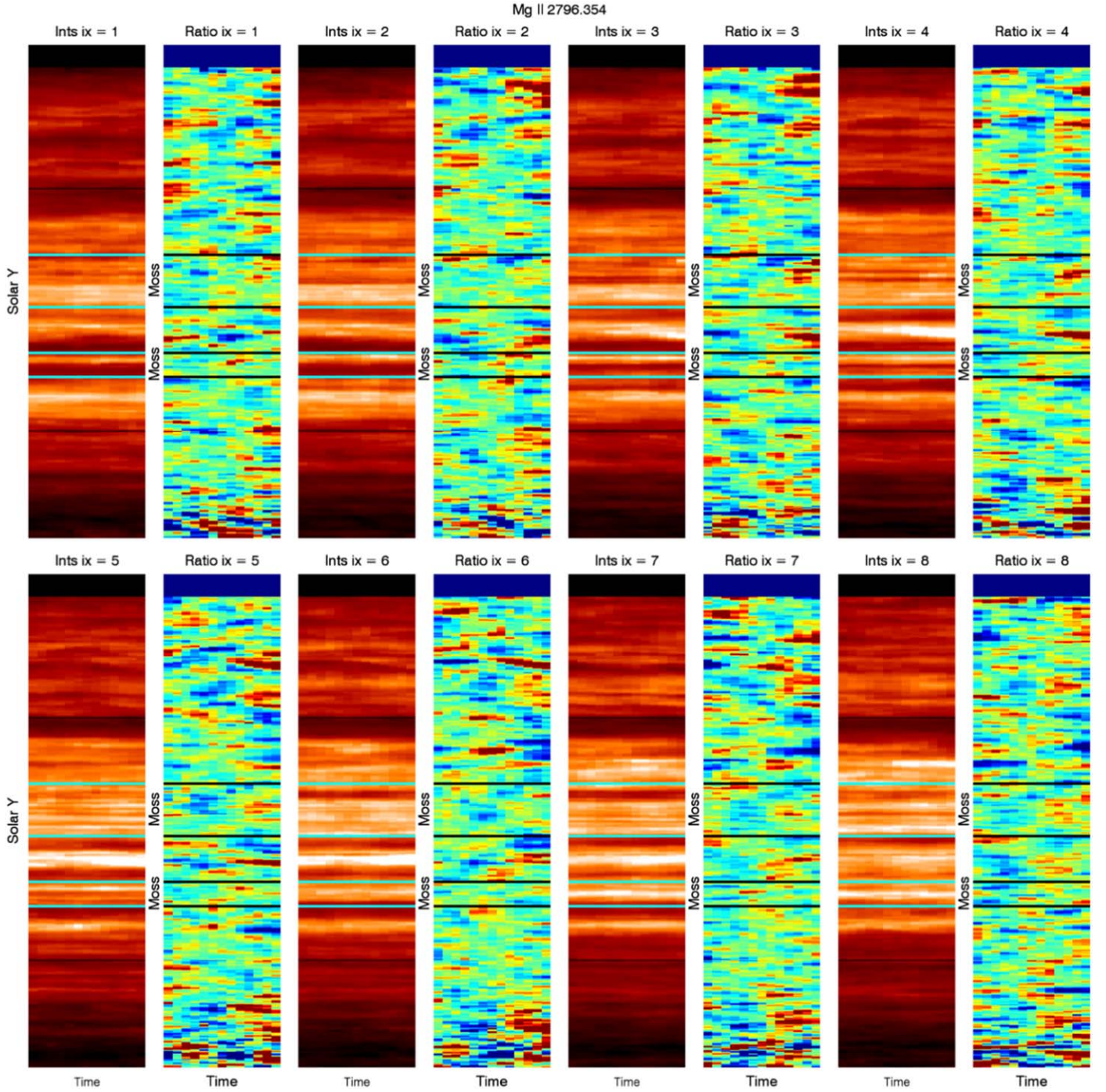
Figure 11. The intensity and variability in Mg II 2796.354 Å as a function of time for each of the eight steps in the IRIS rasters taken during the Hi-C flight. For each step in the raster, the absolute intensity (left panel) and intensity normalized to the row mean (right panel) are shown. The normalized intensities are scaled so that 0.7 is blue and 1.3 is red and indicate strong variability in the moss. The horizontal lines indicate the two large moss regions shown in the box in Figures 5 and 10.

determine which heating scenarios are broadly consistent with the emission measure distribution measured in the active region core and to compare the simulated chromospheric and transition region signatures with what is observed.

To create the heating scenario for each field line, we begin with a steady heating model and assume that the volumetric heating rate on a field line is

$$\epsilon = \epsilon_0 \left(\frac{\bar{B}}{B_0}\right)^{\alpha} \left(\frac{L_0}{L}\right)^{\beta}, \qquad (2)$$

where $\bar{B}$ is the average field along a field line, and L is the total length of the field line. The parameters $B_0 = 76$ G, $L_0 = 29$ Mm, and $\epsilon_0 = 8.77 \times 10^{-3}$ erg cm^{-3} s^{-1} are fixed so that emission measure distribution peaks at approximately 3–4 MK for a typical active region, consistent with the observations. We vary the parameters α and β to optimize the agreement between the details of the simulated and observed DEM. Such steady heating models have been used previously to simulate high-temperature active region emission (e.g., Schrijver et al. 2004; Warren & Winebarger 2006; Winebarger et al. 2008).
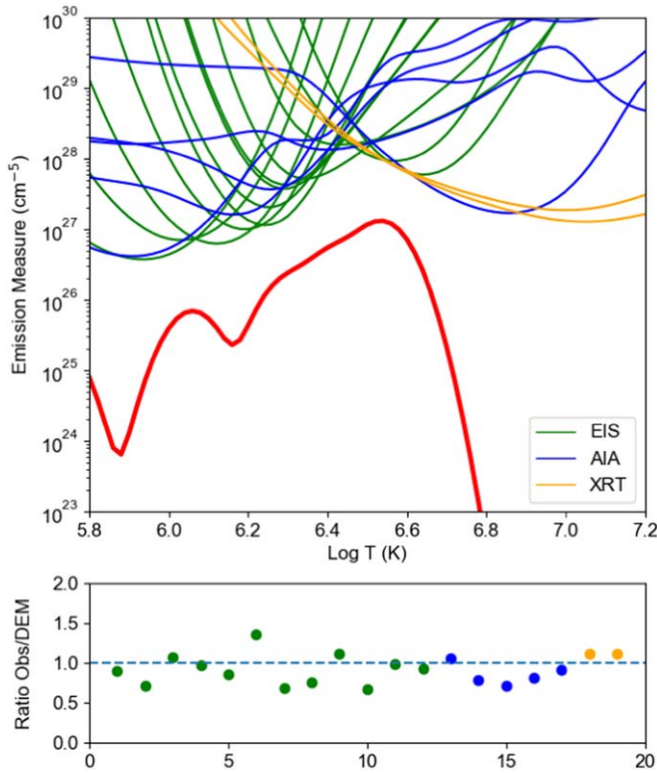
Figure 12. The emission measure distribution in the core of the Hi-C active region. The temperature distribution falls off sharply from its peak near 4 MK. (Top panel) The DEM as a function of temperature derived from the intensities given in Table 1. The curves at the top are the EM loci (observed intensity divided by the response) and form an envelope on the emission measure distribution (red curve). (Bottom panel) The ratio of observed to computed intensity for each line.

To convert the steady heating rate to a time-dependent one, we assume that the distribution of heating event magnitudes depends on two underlying assumptions. The first is that there is a constant probability (p) of a heating event occurring per unit time, i.e., a Poisson process. For $p \sim 1$, we recover steady heating, and for $p \ll 1$, we have low-frequency, impulsive heating. This means that the number of events with a waiting time τ is $N \propto \exp(-p\tau)$. Second we assume that the energy of an event is an exponential function of the waiting time, that is, $E \propto \exp(k\tau)$. Removing τ from these expressions yields,

$$N \propto E^{-p/k}, \qquad (3)$$

or a power law for the distribution of heating event magnitudes with a power-law index of p/k. How to choose the parameter k, which scales the energy to the waiting time, is not clear. We simply assume $k = p/2$ so that the power-law index is -2 in all cases. We stress that this heating scenario is not motivated by physical considerations, but by convenience. This framework allows us to parameterize the heating with a single variable (p) that has a simple interpretation (the probability of an event occurring) into a time-dependent heating function with a property that we expect (a power-law distribution of event magnitudes).

To implement this heating scenario, we fix the duration of the heating and the event probability and then create an unnormalized time series of heating events. Note that each time

series begins with an event. We then normalize the time series so that the mean heating rate corresponds to the magnitude of the steady heating for the field line. We add a small amount of background heating (10^{-5} erg cm^{-3} s^{-1}) to each heating time series. We use the heating time series to compute approximate solutions to the hydrodynamic loop equations using the "enthalpy-based thermal evolution of loops" (EBTEL) model (Klimchuk et al. 2008; Cargill et al. 2012). Some example time series are shown in Figure 13.

To simulate the active region core emission, we use the field lines computed from the NLFF model that pass through the EIS slit (see Figure 6). We loop over each field line using the mean field and loop length to compute the steady heating rate (Equation (2)) and then the time-dependent heating described previously. For each 10 s interval, the heating is determined to be on or off with probability p. The simulation for each field line is run for 10^4 s. At each time step, we bin the values for n_e^2 and normalize the resulting emission measure distribution so that it reproduces the Ca XIV 193.874 Å observed by EIS. We average in time to compute a DEM for comparing with the observations.

To explore parameter space, we consider a range of values, $\alpha, \beta \in [0.2, 0.5, 1.0]$ and $p \in [0.01, 0.05, 0.15, 0.3]$, for a total of 36 simulations. Each pass over all 956 field lines that pass through the EIS slit in the active region core takes about 150 s on a workstation powered by a 3 GHz Intel Xeon W-2150B.

Figure 14 shows emission measure distributions derived from selected simulations where they are compared with the observed DEM shown in Figure 12. As expected, the simulated DEMs are highly sensitive to the frequency of the heating events. For low values of p, large gaps in the heating develop, and there are large departures from equilibrium that show up as a high-temperature component of the DEM. For higher values of p, the departures from equilibrium are rare, and the amount of high-temperature emission is small. Larger values of p are clearly more consistent with the observed temperature distribution.

The search of parameter space also shows that the simulated DEM is also sensitive to the choice of α and β, but this dependence is much weaker. As is illustrated in Figure 14, varying these parameters shifts the peak in the emission measure distribution while leaving its shape relatively constant. The closest match to the observed DEM is for the parameter set $p, \alpha, \beta = (0.3, 0.2, 1.0)$.

It is important to remember that the emission measure distribution itself is highly uncertain (e.g., Testa et al. 2012a; Guennou et al. 2013), particularly at the highest temperatures, and this limits our ability to constrain the simulations. Although some progress has been made recently, there is a clear need for improved observations at temperatures above 5 MK (Winebarger et al. 2008). We will return to this topic in Section 5.

The 0D EBTEL simulations provide a computationally efficient way to estimate the coronal response to time-dependent heating. This is critical for modeling the high-temperature active region core loops, where the emission in an individual loop is difficult to isolate. However, to accurately model the response of the chromosphere and transition region, full hydrodynamic simulations are needed. Such simulations require several orders of magnitude more computing time, so only a relatively small number of loops can be modeled.
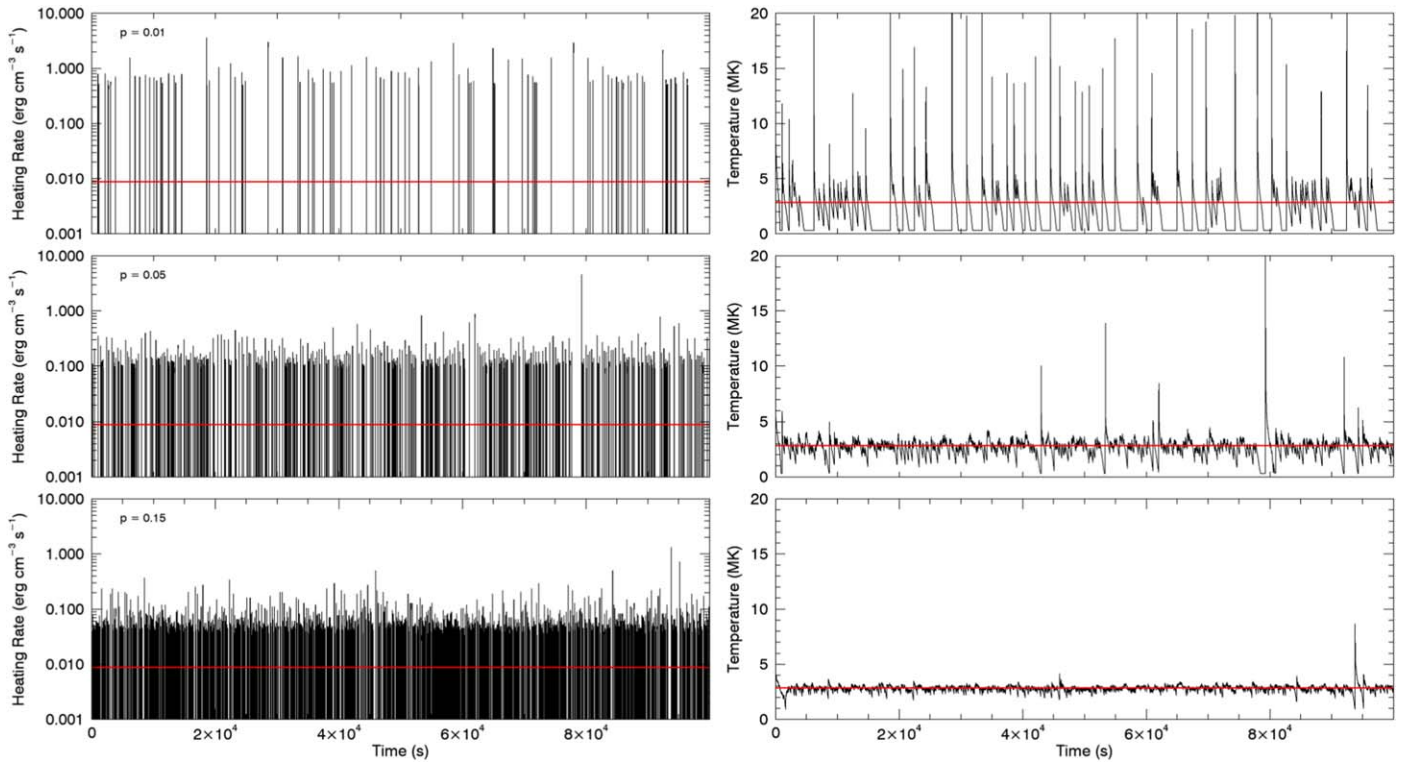
Figure 13. Three examples of heating time series for different values of p. In each case, the time interval is 10 s, the loop length is 29 Mm, and the mean field is 79 G. By combining a constant probability of a heating event per time interval with an exponential dependence of the heating on the waiting time, we create a power-law distribution of event magnitudes. The mean value of each heating time series is the same (8.77×10^{-3} erg cm^{-3} s^{-1}) and indicated by the horizontal red line. The right panels show the corresponding temperatures computed with EBTEL. Here the horizontal red line is the temperature computed using the steady heating rate.

Fortunately, the footpoint emission in the chromosphere and transition region can be represented with a much smaller number of loops, and these simulations are still useful.

We carry out full hydrodynamic simulations using the HYDRAD code (e.g., Bradshaw & Mason 2003; Bradshaw & Cargill 2013). HYDRAD is a modern two-fluid hydrodynamic code that includes nonequilibrium ionization and adaptive mesh refinement along a 1D loop. Furthermore, this code has recently been updated to include the effects of nonlocal thermodynamic equilibrium on the level populations (Reep et al. 2019), making it possible to study the hydrodynamic response of the lower transition region and chromosphere in multi-threaded models.

Three examples of a full hydrodynamic simulation, including radiative transfer in the chromosphere, are shown in Figure 15, where the results for a selected field line, $\alpha = 0.2$, $\beta = 1$, and three different values of p are displayed. For this field line, the loop length is 42 Mm. The heating time series are taken directly from the EBTEL simulation. To compute total event energies, a cross-sectional area of 5×10^{14} cm^{-2} is assumed. For the optically thin Fe IX 171.073 Å line, we compute the line intensity using $\epsilon(T_e, n_e) n_e^2 \, ds$ in each computational cell and only include heights below 3 Mm for one of the footpoints. For the optically thick Mg II 2796.354 Å, we use the radiative transfer code RH1.5D (Uitenbroek 2001; Pereira & Uitenbroek 2015). Mg II is calculated with partial redistribution (PRD) using the "PRD_ANGLE_APPROX" scheme in RH1.5D, and we ran with five atoms: H, He, Mg as active and O, C as passive (i.e., only used as a source of background opacity). We truncate the loop at the size of an IRIS pixel, approximately 240 km on the Sun ($\approx$2.4 Mm of the

42 Mm loop). The intensity calculation for the synthetic profile is identical to that used for the observed profile.

The full simulations indicate that the highly simplified EBTEL simulations are tracking the evolution of the apex temperature and density reasonably well. One notable difference is in the initial evolution ($t < 1000$ s) of the simulations. The EBTEL simulations begin with the loop in equilibrium with an apex temperature of 3–4 MK and a relatively high density. For the HYDRAD simulations, we use VAL-C for the initial chromosphere, so the initial loop atmosphere is tenuous. These simulations illustrate the critical role that the initial conditions play in the response of the loop to heating. It is only for relatively intense heating and a tenuous initial atmosphere that we see a strong chromospheric and transition region response to nanoflare-sized heating events. A similar conclusion was reached by Polito et al. (2018), who studied the deposition of energy from beam and uniform heating scenarios into loops with various initial temperatures. For hot, dense initial atmospheres, their simulations indicate no transition region heating for events of typical nanoflare energies.

The high-frequency heating scenarios that are most consistent with the observed emission measure distribution lead to relatively weak heating on loops that are generally hot and dense. This significantly attenuates the response of the chromosphere and transition region to heating events. Finally, for these simulations, we have not calculated nonequilibrium ionization. This has been shown to strongly influence the interpretation of high-temperature line emission (e.g., Bradshaw & Cargill 2006; Reale & Orlando 2008; Barnes et al. 2016). However, for the relatively high-density loops produced by high-frequency heating, this is likely to be much less important.
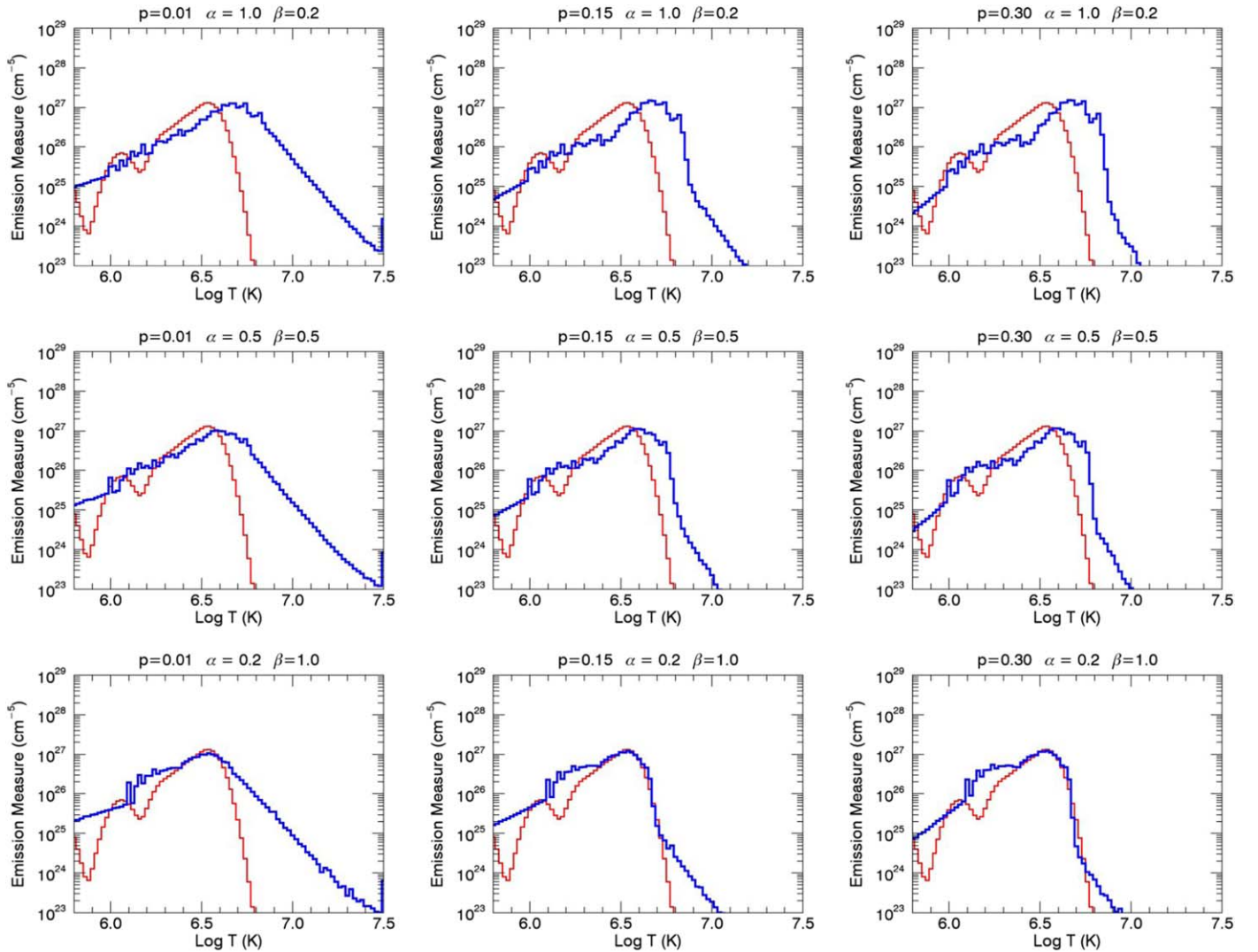
Figure 14. Examples of simulated and observed emission measures for various combinations of p, α, and β. The three values of p represent low-, medium-, and high-frequency heating scenarios. The red line in each plot is the observed DEM, and the blue line is the DEM computed from the simulation. The parameter set (0.3, 0.2, 1.0) provides the best match to the observed DEM, although this conclusion is dependent on the behavior of the DEM above $\log T = 6.8$, which is very uncertain.

5. Summary and Discussion

We have investigated the properties of the active region moss using observations taken during the Hi-C flight of 2018 May 29. Despite the high cadence and high spatial resolution of the Hi-C images, there is little evidence for impulsive heating events in the moss in these data. Measurements from EIS, AIA, and XRT show that the DEM in the active region core loops is sharply peaked at about 4 MK, consistent with many previous analysis. Furthermore, we have constructed a time-dependent heating scenario using magnetic field parameters computed from a magnetic field extrapolation and the assumption of a Poisson waiting time distribution. High-frequency heating provides the best match between the simulated and observed DEM. Taken together, these observational and modeling results provide compelling evidence that the heating in the active region core is taking place at a relatively high frequency and that these loops are close to equilibrium. There is some evidence for variability in the Mg II 2796.354 Å line observed by IRIS, but it is difficult to link this variability to coronal activity. Full hydrodynamic simulations suggest that the high-frequency heating scenarios investigated here would generally produce very weak signatures in the lower transition region and chromosphere.

Perhaps the weakest link in this analysis is using the active region core DEM to constrain the time-dependent heating scenarios. As mentioned previously, the sparseness of spectrally resolved emission formed at temperatures above 5 MK in combination with the uncertainties in the instrument calibration and the atomic data make the calculation of the DEM at high temperatures very difficult. Our DEM calculations clearly indicate that a very low-frequency heating scenario is inconsistent with the observations, but they cannot discriminate between moderate- and high-frequency cases (e.g., $p = 0.15$ versus $p = 0.3$).

We stress, however, that most DEM calculations in the active region core suggest relatively steep temperature distributions. The recent analysis by Ishikawa & Krucker (2019), who concluded that "The hot component has a rather small emission measure ($\sim$0.1% of the total EM is above 5 MK)," is particularly important, since they used spectrally resolved observations of the soft X-ray continuum, which are very sensitive to temperature. Also, since the continuum reflects the electron temperature directly, it is not likely to be strongly influenced by nonequilibrium ionization effects.
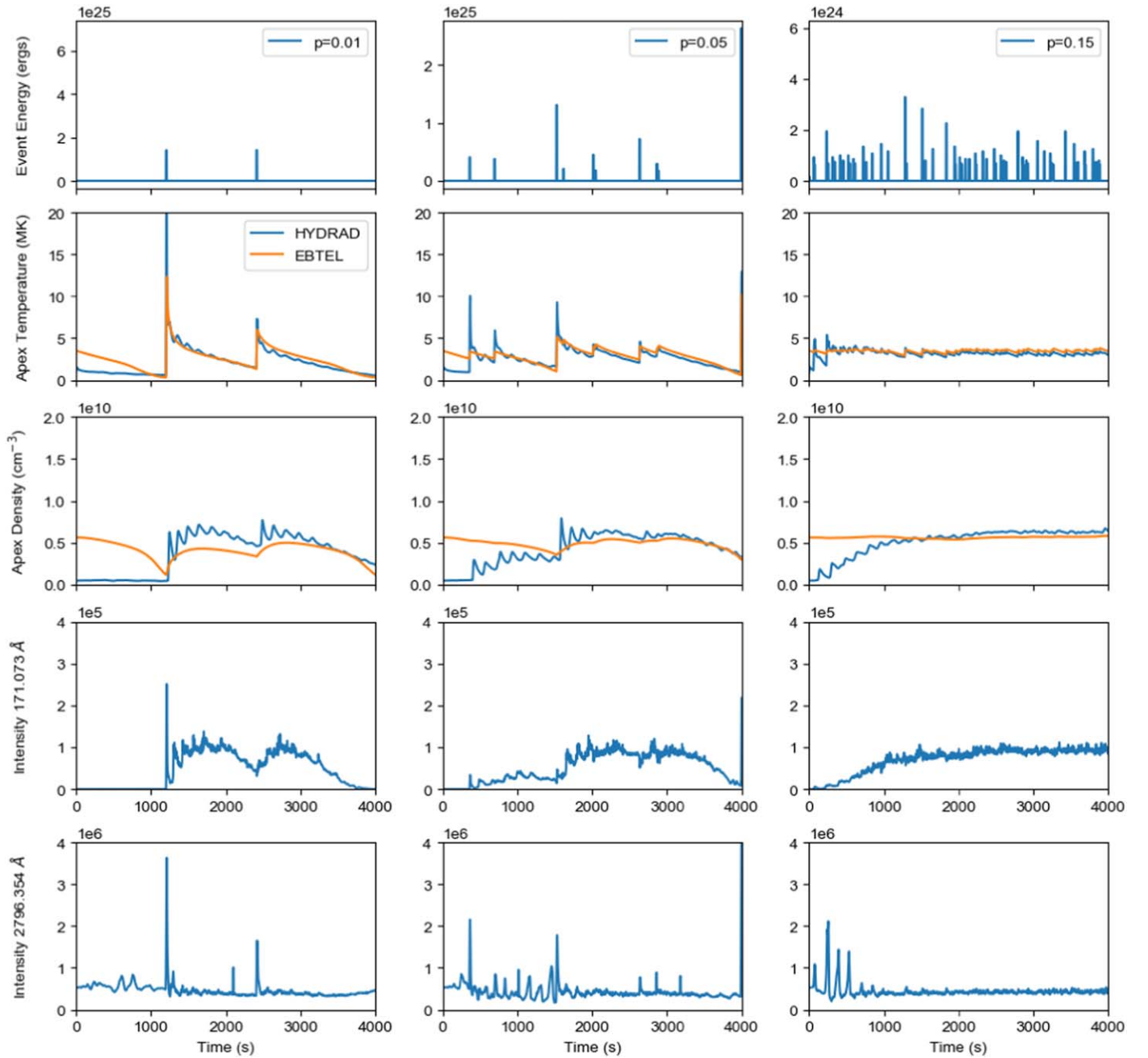
Figure 15. Example EBTEL and NLTE HYDRAD simulations for a selected field line. Each column shows the simulation for a different value of p, the heating event probability per unit time. The top panels show the total event energy as a function of time and the resulting electron density and temperature averaged over the loop apex. The bottom two rows of panels show the simulated intensity in Fe IX 171.073 Å and Mg II 2796.354 Å with units of erg cm^{-2} s^{-1} sr^{-1}. A strong transition region and chromospheric response is seen only for large heating events on relatively tenuous loops.

The short duration of the Hi-C flight is another limitation of this study since it makes it difficult to apply more sophisticated event detection algorithms. A recent automatic analysis of moss transient events using extended time series of AIA data shows that the level of moss variability can fluctuate significantly over timescales of minutes to tens of minutes (Graham et al. 2019).

Finally, we emphasize that high frequency should not be taken as a synonym for steady. It is clear from the inspection of AIA Fe XVIII movies (Ugarte-Urra & Warren 2014), through detailed analysis (Cargill 2014), and physical considerations (Klimchuk 2006) that the heating cannot be truly steady. The high-frequency scenario that we advocate here allows for occasional departures from equilibrium that would be

detectable as heating events, such as those observed with Hi-C and IRIS by Testa et al. (2013, 2014, 2020). However, it is also possible that such events are related to other processes, such as flux cancellation (e.g., Tiwari et al. 2014, 2019; Chitta et al. 2018; Wang et al. 2019), and are not part of the same distribution of heating events that give rise to the quiescent, active region core loops. Observations with the Daniel K. Inouye Solar Telescope (Tritschler et al. 2016) will help to clarify the role of mixed polarity in the dynamics of the moss.

ORCID iDs

Harry P. Warren https://orcid.org/0000-0001-6102-6851
Jeffrey W. Reep https://orcid.org/0000-0003-4739-1152
Ignacio Ugarte-Urra https://orcid.org/0000-0001-5503-0491
David H. Brooks https://orcid.org/0000-0002-2189-9313
Amy R. Winebarger https://orcid.org/0000-0002-5608-531X
Sabrina Savage https://orcid.org/0000-0002-6172-0517
Bart De Pontieu https://orcid.org/0000-0002-8370-952X
Hardi Peter https://orcid.org/0000-0001-9921-0937
Jonathan W. Cirtain https://orcid.org/0000-0002-2941-5782
Leon Golub https://orcid.org/0000-0001-9638-3082
Richard Morton https://orcid.org/0000-0001-5678-9002
Laurel Rachmeler https://orcid.org/0000-0002-3770-009X
Paola Testa https://orcid.org/0000-0002-0405-0668
Sanjiv Tiwari https://orcid.org/0000-0001-7817-2978

References

Antiochos, S. K., Karpen, J. T., DeLuca, E. E., Golub, L., & Hamilton, P. 2003, ApJ, 590, 547
Aschwanden, M. J. 2016, ApJS, 224, 25
Aschwanden, M. J., Nightingale, R. W., & Alexander, D. 2000, ApJ, 541, 1059
Asgari-Targhi, M., & van Ballegooijen, A. A. 2012, ApJ, 746, 81
Barnes, W. T., Cargill, P. J., & Bradshaw, S. J. 2016, ApJ, 829, 31
Berger, T. E., de Pontieu, B., Fletcher, L., et al. 1999, SoPh, 190, 409
Bingert, S., & Peter, H. 2011, A&A, 530, A112
Boerner, P. F., Testa, P., Warren, H., Weber, M. A., & Schrijver, C. J. 2014, SoPh, 289, 2377
Bradshaw, S. J., & Cargill, P. J. 2006, A&A, 458, 987
Bradshaw, S. J., & Cargill, P. J. 2013, ApJ, 770, 12
Bradshaw, S. J., & Mason, H. E. 2003, A&A, 401, 699
Brooks, D. H., Warren, H. P., & Ugarte-Urra, I. 2012, ApJL, 755, L33
Byrd, R., Lu, P., Nocedal, J., & Zhu, C. 1995, SIAM J. Sci. Comput., 16, 1190
Cargill, P. J. 1994, ApJ, 422, 381
Cargill, P. J. 2014, ApJ, 784, 49
Cargill, P. J., Bradshaw, S. J., & Klimchuk, J. A. 2012, ApJ, 752, 161
Cargill, P. J., Warren, H. P., & Bradshaw, S. J. 2015, RSPTA, 373, 20140260
Chitta, L. P., Peter, H., & Solanki, S. K. 2018, A&A, 615, L9
Courrier, H., Kankelborg, C., De Pontieu, B., & Wülser, J.-P. 2018, SoPh, 293, 125
Culhane, J. L., Harra, L. K., James, A. M., et al. 2007, SoPh, 243, 19
Dahlburg, R. B., Einaudi, G., Taylor, B. D., et al. 2016, ApJ, 817, 47
De Pontieu, B., Title, A. M., Lemen, J. R., et al. 2014, SoPh, 289, 2733
Del Zanna, G. 2013a, A&A, 558, A73
Del Zanna, G. 2013b, A&A, 555, A47

Del Zanna, G. 2014, A&A, 565, A14
Del Zanna, G., & Mason, H. E. 2003, A&A, 406, 1089
Del Zanna, G., Tripathi, D., Mason, H., Subramanian, S., & O'Dwyer, B. 2015, A&A, 573, A104
Dere, K. P., Del Zanna, G., Young, P. R., Landi, E., & Sutherland, R. S. 2019, ApJS, 241, 22
Feldman, U. 1992, PhyS, 46, 202
Freeland, S. L., & Handy, B. N. 1998, SoPh, 182, 497
Golub, L., Deluca, E., Austin, G., et al. 2007, SoPh, 243, 63
Graham, D. R., De Pontieu, B., & Testa, P. 2019, ApJL, 880, L12
Grigis, P., Su, Y., & Weber, M. 2012, AIA PSF Characterization and Image Deconvolution, Tech. Rep., LMSAL
Gudiksen, B. V., & Nordlund, Å. 2005, ApJ, 618, 1020
Guennou, C., Auchère, F., Klimchuk, J. A., Bocchialini, K., & Parenti, S. 2013, ApJ, 774, 31
Handy, B. N., Acton, L. W., Kankelborg, C. C., et al. 1999, SoPh, 187, 229
Hansteen, V., Guerreiro, N., De Pontieu, B., & Carlsson, M. 2015, ApJ, 811, 106
Ishikawa, S.-n., & Krucker, S. 2019, ApJ, 876, 111
Kigure, H., Takahashi, K., Shibata, K., Yokoyama, T., & Nozawa, S. 2010, PASJ, 62, 993
Klimchuk, J. A. 2006, SoPh, 234, 41
Klimchuk, J. A., Patsourakos, S., & Cargill, P. J. 2008, ApJ, 682, 1351
Kobayashi, K., Cirtain, J., Winebarger, A. R., et al. 2014, SoPh, 289, 4393
Lemen, J. R., Title, A. M., Akin, D. J., et al. 2012, SoPh, 275, 17
Lenz, D. D., DeLuca, E. E., Golub, L., Rosner, R., & Bookbinder, J. A. 1999, ApJL, 517, L155
Mitra-Kraev, U., & Del Zanna, G. 2019, A&A, 628, A134
Pereira, T. M. D., & Uitenbroek, H. 2015, A&A, 574, A3
Polito, V., Testa, P., Allred, J., et al. 2018, ApJ, 856, 178
Rachmeler, L. A., Winebarger, A. R., Savage, S. L., et al. 2019, SoPh, 294, 174
Reale, F. 2014, LRSP, 11, 4
Reale, F., & Orlando, S. 2008, ApJ, 684, 715
Reep, J. W., Bradshaw, S. J., Crump, N. A., & Warren, H. P. 2019, ApJ, 871, 18
Saba, J. L. R., & Strong, K. T. 1986, AdSpR, 6, 37
Scherrer, P. H., Schou, J., Bush, R. I., et al. 2012, SoPh, 275, 207
Schmelz, J. T., Saba, J. L. R., Ghosh, D., & Strong, K. T. 1996, ApJ, 473, 519
Schrijver, C. J., Sandman, A. W., Aschwanden, M. J., & De Rosa, M. L. 2004, ApJ, 615, 512
Teriaca, L., Warren, H. P., & Curdt, W. 2012, ApJL, 754, L40
Testa, P., De Pontieu, B., Allred, J., et al. 2014, Sci, 346, 1255724
Testa, P., De Pontieu, B., Martínez-Sykora, J., et al. 2013, ApJL, 770, L1
Testa, P., De Pontieu, B., Martínez-Sykora, J., Hansteen, V., & Carlsson, M. 2012a, ApJ, 758, 54
Testa, P., Drake, J. J., & Landi, E. 2012b, ApJ, 745, 111
Testa, P., Polito, V., & Pontieu, B. D. 2020, ApJ, 889, 124
Testa, P., & Reale, F. 2012, ApJL, 750, L10
Tiwari, S. K., Alexander, C. E., Winebarger, A. R., & Moore, R. L. 2014, ApJL, 795, L24
Tiwari, S. K., Panesar, N. K., Moore, R. L., et al. 2019, ApJ, 887, 56
Tiwari, S. K., Thalmann, J. K., Panesar, N. K., Moore, R. L., & Winebarger, A. R. 2017, ApJL, 843, L20
Tritschler, A., Rimmele, T. R., Berukoff, S., et al. 2016, AN, 337, 1064
Ugarte-Urra, I., & Warren, H. P. 2014, ApJ, 783, 12
Uitenbroek, H. 2001, ApJ, 557, 389
van Ballegooijen, A. A., Asgari-Targhi, M., Cranmer, S. R., & DeLuca, E. E. 2011, ApJ, 736, 3
van Ballegooijen, A. A., Asgari-Targhi, M., & Voss, A. 2017, ApJ, 849, 46
Wang, Y. M., Ugarte-Urra, I., & Reep, J. W. 2019, ApJ, 885, 34
Warren, H. P., Brooks, D. H., Doschek, G. A., & Feldman, U. 2016, ApJ, 824, 56
Warren, H. P., Brooks, D. H., & Winebarger, A. R. 2011, ApJ, 734, 90
Warren, H. P., Byers, J. M., & Crump, N. A. 2017, ApJ, 836, 215
Warren, H. P., Crump, N. A., Ugarte-Urra, I., et al. 2018, ApJ, 860, 46
Warren, H. P., Ugarte-Urra, I., Doschek, G. A., Brooks, D. H., & Williams, D. R. 2008, ApJL, 686, L131
Warren, H. P., Ugarte-Urra, I., & Landi, E. 2014, ApJS, 213, 11
Warren, H. P., & Winebarger, A. R. 2006, ApJ, 645, 711
Warren, H. P., Winebarger, A. R., & Brooks, D. H. 2012, ApJ, 759, 141
Wiegelmann, T. 2004, SoPh, 219, 87
Winebarger, A. R., Warren, H. P., & Falconer, D. A. 2008, ApJ, 676, 672
Woods, T. N., Eparvier, F. G., Hock, R., et al. 2012, SoPh, 275, 115
Zhu, C., Byrd, R. H., Lu, P., & Nocedal, J. 1997, ACM Trans. Math. Softw., 23, 550